

Remote Breathing Monitoring Using LiDAR Technology

Omar Rinchi
Missouri University of
Science and Technology
Rolla, MO, USA
Email: omar.rinchi@mst.edu

Ahmad Alsharoa
Missouri University of
Science and Technology
Rolla, MO, USA
Email: aalsharoa@mst.edu

Denise A. Baker
Missouri University of
Science and Technology
Rolla, MO, USA
Email: bakerden@mst.edu

Abstract—Breathing monitoring is crucial in healthcare for early detection of health issues, but traditional methods face challenges like invasiveness, privacy concerns, and limited applicability in daily settings. This paper introduces light detection and ranging (LiDAR) sensors as a remote, privacy-respecting alternative for monitoring breathing metrics, including inhalation/exhalation patterns, respiratory rates, breath depth, and detecting breathlessness. We highlight LiDAR’s ability to function across various postures, presenting empirical evidence of its accuracy and reliability. Our findings position LiDAR as an innovative solution in breathing monitoring, offering significant advantages over conventional methods.

Index Terms—light detection and ranging (LiDAR), apnea, breathing, healthcare, and respiratory rate.

I. INTRODUCTION

Breathing monitoring emerges as a powerful tool for early health detection and management, capturing essential metrics like respiratory rate and tidal volume. It shines in everyday settings, alerting to anomalies that may indicate health issues, from sleep apnea and stress to potential respiratory infections [1]. By offering real-time insights, it empowers individuals to act swiftly, fostering proactive health practices. This not only transforms medical care but also enhances daily well-being, making a significant impact on life quality.

Breathing monitoring technologies fall into invasive, non-invasive, and remote categories. Invasive methods, like the arterial blood gas (ABG) analysis and tracheal intubation, offer high precision but are uncomfortable and restricted to medical settings [2]. Non-invasive techniques use external devices like chest straps and smart textiles [3], which are user-friendly but can be cumbersome and socially awkward for continuous wear [4]. Remote monitoring, utilizing technologies like thermal and RGB-D depth cameras, captures breathing data without physical contact, offering a less intrusive option for continuous observation [5], [6].

Remote breathing monitoring, while advantageous for its passive, non-intrusive tracking and comfort, faces significant challenges that impact its efficacy. Environmental factors like ambient temperature and lighting conditions critically influence the accuracy of technologies such as thermal and RGB-D sensors. For example, thermal cameras struggle with dynamic activities due to temperature variability [7], and RGB-D sensors perform poorly in low light or direct sunlight. Moreover, these technologies face limitations in detecting dark colors, potentially leading to biased outcomes against

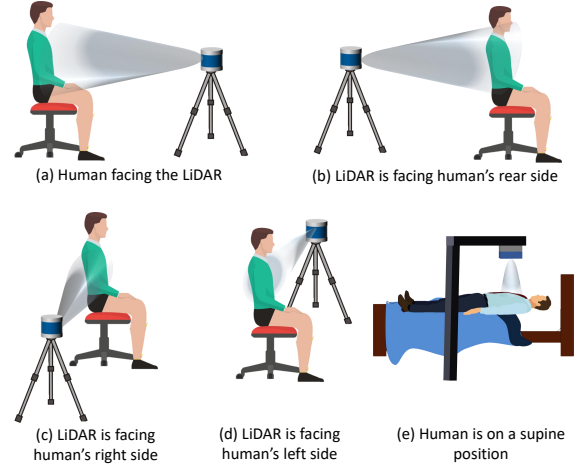


Fig. 1: The proposed system scenario and experimental setup. individuals with darker skin tones [8], [9]. Privacy concerns also emerge with the use of video and thermal cameras, posing ethical considerations [10].

We present LiDAR technology as a robust solution to traditional breathing monitoring challenges, leveraging laser light for remote sensing and generating 3D mappings without being influenced by ambient temperature, lighting, or object color and texture. This color-blind approach avoids potential color discrimination and enhances privacy by minimizing the risk of identifying personal features through sparse LiDAR-generated point clouds [11]. LiDAR’s versatility is demonstrated in healthcare applications, from activity recognition using deep-learning [12] to estimating tidal volume in patients [13], [14], showcasing its potential for remote, privacy-preserving monitoring in diverse settings.

This study explores LiDAR’s capability to monitor various respiratory metrics, extending beyond the tidal volume estimation in supine subjects as seen in previous research [13], [14]. We broaden our investigation by (i) utilizing LiDAR for detailed breathing analysis, including tracking inhalation/exhalation patterns, estimating respiratory rate, assessing breath depth, and detecting breathlessness episodes; and (ii) showcasing LiDAR’s adaptability in monitoring breathing across different postures, not limited to lying down positions.

II. SYSTEM SCENARIO AND EXPERIMENTAL SETUP

In this study, our objective is to explore the potential of the LiDAR sensor in capturing vital breathing moments from

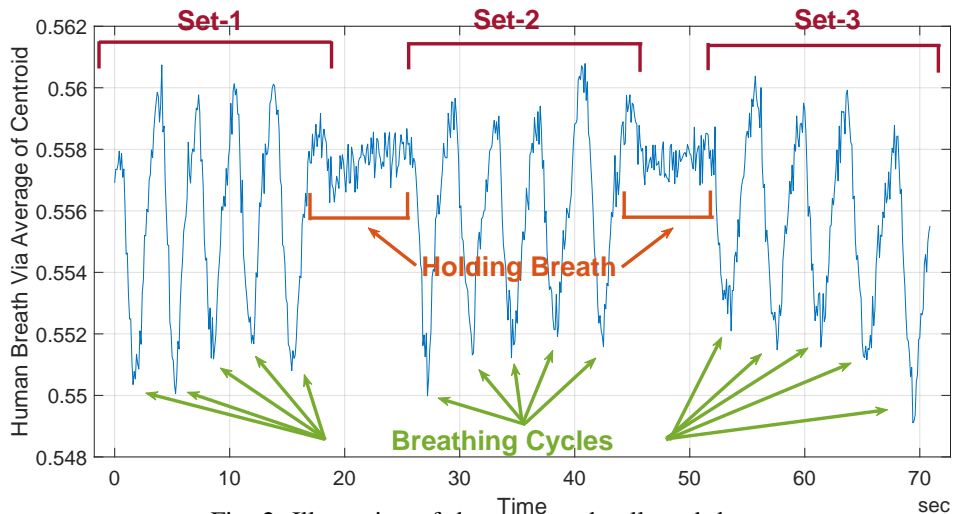


Fig. 2: Illustration of the processed collected data.

various angles. We crafted five distinct experimental scenarios to see how the sensor performs under different conditions, all of which are illustrated in Fig. 1.

In Scenario-a, the participant was seated upright with the LiDAR sensor directly in front, focusing on frontal torso data. Scenario-b also had the participant seated, but with the LiDAR behind them to assess differences in data from this angle. For Scenario-c and Scenario-d, the LiDAR was placed to the right and left sides, respectively, to examine lateral breathing patterns. Scenario-e involved the participant lying supine with the LiDAR positioned overhead, offering a unique overhead perspective. All seated scenarios used a backless chair to maintain clear line-of-sight between the participant and the LiDAR, and the participant wore a T-shirt for consistency. The LiDAR was kept at a fixed distance of 2 meters from the participant in every setup. In our experimental procedure, the participant performs three sets of breathing cycles, each set comprising five breaths¹ After completing each set, the participant pauses and holds breath for a designated period, simulating instances when breathing stops. The duration of each scenario is approximately 1.25 minutes, and each breath-holding phase spans about 10 seconds.

Following each experiment, we carefully gather and securely store the data for detailed analysis. Fig. 2 illustrates a sample of the processed data from Scenario-a, displayed over time. A comprehensive explanation of our data processing techniques is discussed in Section III. In Fig. 2, we identify three distinct sets of breathing patterns, marked in red. Between these sets, periods of breath-holding are indicated in orange. Upon closer inspection, each set contains five individual breathing cycles, each denoted by green arrows.

III. METHODOLOGY

Utilizing the data gathered from the five scenarios, our aim is to process this data to extract essential breathing parameters. Our objectives are fourfold: (i) continuously tracking inhalation/exhalation patterns over time, (ii) estimating the

¹A 'breath' is defined as one inhalation followed by one exhalation, so each set involves five successive inhale-exhale cycles.

respiratory rate, (iii) measuring the amplitude or depth of breaths, and (iv) detect any pauses or gaps in breathing.

A. Pre-processing

The raw LiDAR collected data consists of T time frames, such that the frame $n_t \in \mathcal{N}$ where $\mathcal{N} = \{n_1, n_2, \dots, n_t, \dots, n_T\}$ consists of I points where each point $p_i[n_t]$ in the point cloud is defined using its coordinates such that $p_i[n_t] = [x_i[n_t], y_i[n_t], z_i[n_t]]^T$.

We start our analysis by conducting some pre-processing on the collected LiDAR raw data to convert it into a format like the one shown in Fig. 2. In this new format, the data is plotted against time such that each peak or notch in the graph corresponds to a specific breath cycle, which includes both inhalation and exhalation. Once we achieve this format, we will process the newly formatted data so that it is possible to accurately identify each breathing metric.

The initial step in our process involves data filtration, where we aim to isolate only the relevant point cloud data associated with the human's torso. Essentially, we want to extract the points related to the torso area and discard all others. An example of this procedure, applied to the data from Scenario-a, can be seen in Fig. 3. This illustration focuses solely on the participant's chest region. Different techniques can be utilized to achieve this targeted filtration; for instance, we have demonstrated in [12] a deep-learning approach to segment human body parts utilizing a stand-alone 3D LiDAR sensor. Leveraging this technique, we can discern various body sections, thereby segmenting the torso region. The authors in [14] address this issue by employing reflective markers worn by humans. Reflective markers can be used to identify torso region. In this work, we utilize a region of interest (ROI)-based approach where we define a boundary region such that any point cloud outside this region is filtered. More specifically, let $\mathcal{P}[n_t]$ be the set of all I point cloud data captured by the LiDAR at frame n_t (i.e., $\mathcal{P}[n_t] = \{p_1[n_t], p_2[n_t], \dots, p_i[n_t], \dots, p_I[n_t]\}$, $\forall n_t \in \mathcal{N}$). Let $\mathcal{J}[n_t]$ represent the defined spatial boundaries of the human torso, such that any point $p_i[n_t] \in \mathcal{P}[n_t]$ with coordinates $(x_i[n_t], y_i[n_t], z_i[n_t])$ within $\mathcal{J}[n_t]$ belongs to the chest or

abdominal regions. The region $\mathcal{T}[n_t]$ can be defined based on threshold values as

$$\begin{aligned} x_{th1} \leq x_i[n_t] \leq x_{th2}; \quad y_{th1} \leq y_i[n_t] \leq y_{th2}; \\ z_{th1} \leq z_i[n_t] \leq z_{th2}, \end{aligned} \quad (1)$$

where $x_{th1}, x_{th2}, y_{th1}, y_{th2}, z_{th1}$, and z_{th2} are the thresholds that defines the ROI. Then, the filtered point cloud data $\mathcal{F}[n_t]$ in frame n_t are given by

$$\mathcal{F}[n_t] = \mathcal{P}[n_t] \cap \mathcal{T}[n_t], \quad (2)$$

where the new filtered data set $\mathcal{F}[n_t]$ consists of E points, i.e., $\mathcal{F}[n_t] = \{p_1^F[n_t], p_2^F[n_t], \dots, p_e^F[n_t], \dots, p_E^F[n_t]\}$ such that $p_e^F[n_t] = [x_e^F[n_t], y_e^F[n_t], z_e^F[n_t]]^T$. The boundary set $\mathcal{T}[n_t]$ can be configured in one of two ways: it can remain stationary, reflecting empirical domain knowledge (e.g., when a human lies on a bed with the LiDAR positioned above the torso), or it can be dynamically adjusted using a torso tracking mechanism [15]. In this work, we follow the stationary approach.

The subsequent step involves converting the data to a format that better captures breathing patterns over time. This involves leveraging the geometric shifts that arise during the breathing process and charting these changes over time. Our approach begins with selecting a representative point, $P^*[n_t]$, from the filtered human torso dataset $\mathcal{F}[n_t]$. While there are various methods to pinpoint this representative point, we opt for the centroid of the filtered human torso dataset. Our preference for the centroid is grounded in its robustness to outliers, ensuring a more accurate representation even if the data filtering isn't flawless. Accordingly, we define the representative point, $P^*[n_t]$ as

$$\begin{aligned} P^*[n_t] = \{C^x[n_t], C^y[n_t], C^z[n_t]\}, \quad \text{where} \\ C^x[n_t] = E^{-1} \sum_{e=1}^E x_e^F[n_t]; \quad C^y[n_t] = E^{-1} \sum_{e=1}^E y_e^F[n_t]; \\ C^z[n_t] = E^{-1} \sum_{e=1}^E z_e^F[n_t]. \end{aligned} \quad (3)$$

Now, it is possible to capture human breaths by inspecting the changes in the values of $C^x[n_t], C^y[n_t], C^z[n_t]$. To visualize these variations, one approach is to plot specific coordinate components of $P^*[n_t]$ against time — for instance, plotting $C^x[n_t]$ versus the corresponding frames $n_t \in \mathcal{N}$.

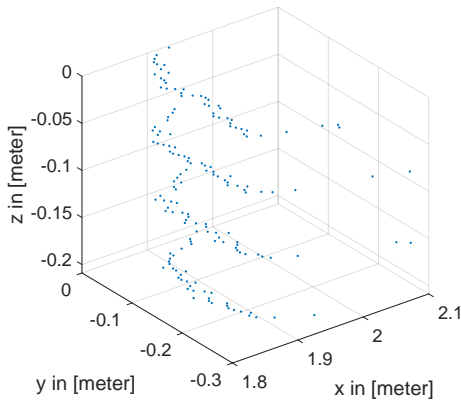


Fig. 3: Human torso point cloud after filtering the raw data.

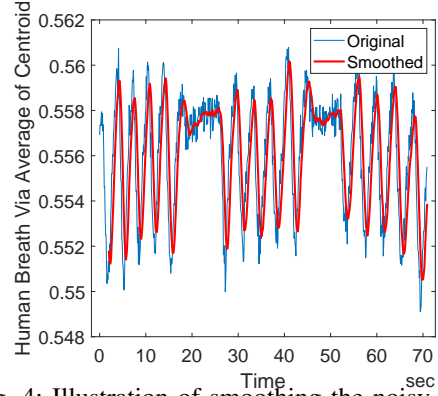


Fig. 4: Illustration of smoothing the noisy data.

Additionally, an alternative method involves computing the mean value of the three centroid coordinates and charting this average against time, represented as $\frac{C^x[n_t] + C^y[n_t] + C^z[n_t]}{3}$ versus the corresponding frames $n_t \in \mathcal{N}$. The choice of the utilized approach depends on the orientation of the human with respect to the LiDAR sensor. Formatting the data against specific coordinate components requires the knowledge of the orientation of the human with respect to the LiDAR but can yield higher sensitivity to capture the inhalation/exhalation cycle, while formatting the data against the average of the centroid can ensure a generic solution that is independent of the human orientation but will yield lower sensitivity to capture the breath compared to the former approach.

B. Breath Monitoring

Based on the established methodology, we can now generate a breath-versus-time plot akin to Fig. 2. The subsequent task involves identifying human breaths from the presented data. Notably, the peaks in the diagram align with human chest displacements. Yet, as illustrated in Fig. 2, the inherent noise in the data—attributable to LiDAR's acute sensitivity to chest movements—complicates peak detection. To address this challenge, we introduce a data smoothing technique using a moving average filter. This transforms the data into a more streamlined representation, comparable to the red curve in Fig. 4. The mathematical representation for the moving average filter is as follows

$$y_{\text{smoothed}}[n_t] = 1/M \sum_{m=0}^{M-1} y[n_t - m], \quad \forall n_t \in \mathcal{N}, \quad (4)$$

where M is the length of the moving average window (number of frames to average over), m is the summation index, representing the samples within the window, $y[n_t - m]$ is un-smoothed data at frame n_t , and $y_{\text{smoothed}}[n_t]$ is the output smoothed data. The ability to accurately track inhalation and exhalation patterns over time is essential for understanding specific events of the breath cycle. Towards this end, the first step is to detect the peaks within the smoothed breath data, as they correspond to these breath cycle events. For this task, we employed a straightforward yet effective local minimums detection technique. This method is mainly rooted in pinpointing data points that exhibit values higher than their immediate neighbors.

However, to further refine our results and improve accuracy, we introduced an additional filtering step. Instead of relying

exclusively on the initial set of detected peaks, we filter out local minimums (given that in our data, breath events manifest as negative peaks) that fall above the average value of the smoothed data. The underlying rationale is that notable breath events are typically characterized by pronounced troughs, which are deeper than the average of the entire data set. Considering that $\mathcal{B} = \{b[\tilde{n}_1], b[\tilde{n}_2], \dots, b[\tilde{n}_k], \dots, b[\tilde{n}_K]\}$ is a set comprising the amplitudes of the detected peaks from the smoothed data and $\tilde{\mathcal{N}} = \{\tilde{n}_1, \tilde{n}_2, \dots, \tilde{n}_k, \dots, \tilde{n}_K\}$ is a set containing their corresponding frame numbers, the filtered set $\bar{\mathcal{B}} = \{\bar{b}[\bar{n}_1], \bar{b}[\bar{n}_2], \dots, \bar{b}[\bar{n}_s], \dots, \bar{b}[\bar{n}_S]\}$ and its respective frame set $\bar{\mathcal{N}} = \{\bar{n}_1, \bar{n}_2, \dots, \bar{n}_s, \dots, \bar{n}_S\}$ can be defined as

$$\bar{\mathcal{B}} = \{b[\tilde{n}_t] \mid b[\tilde{n}_t] \leq \frac{1}{T} \sum_{n_t=1}^T y_{\text{smoothed}}[n_t], \forall \tilde{n}_t \in \tilde{\mathcal{N}}, n_t \in \mathcal{N}\},$$

$$\bar{\mathcal{N}} = \{\tilde{n}_t \mid b[\tilde{n}_t] \leq \frac{1}{T} \sum_{n_t=1}^T y_{\text{smoothed}}[n_t], \forall \tilde{n}_t \in \tilde{\mathcal{N}}, n_t \in \mathcal{N}\}. \quad (5)$$

Accordingly, the breathing patterns can be tracked using $\bar{\mathcal{N}}$ while we account for $\bar{\mathcal{B}}$ to monitor the breathing depth.

Following the identification of breath cycle events, the next imperative step is to quantify the respiratory rate, a measure which plays a pivotal role in many clinical and physiological assessments. The respiratory rate, denoted as R , represents the number of complete inhalation-exhalation cycles an individual completes in a minute. Given the detected breathing events denoted by the set $\bar{\mathcal{B}}$, the respiratory rate can thus be estimated as

$$R = \frac{\text{card}(\bar{\mathcal{B}})}{\tau} \times 60, \quad (6)$$

where $\text{card}(\cdot)$ refers to the cardinality (or count) of a set (i.e., the number of elements in a set), and τ is measurement time in seconds. The last breathing metric that is to be identified is the episodes of breathlessness. We define this metric as the set that includes the frames in which a human was not breathing, i.e., $\hat{\mathcal{N}} = \{\hat{n}_1, \hat{n}_2, \dots, \hat{n}_g, \hat{n}_G\}$ where $\hat{\mathcal{N}} \in \mathcal{N}$ and $\bar{\mathcal{N}} \cap \hat{\mathcal{N}} = \emptyset$. For this purpose, we estimate $\hat{\mathcal{N}}$ using a moving variance, more specifically, we start by computing the moving variance for every point as

$$v[n_t] = \frac{1}{W-1} \sum_{u=n_t-\lfloor \frac{W-1}{2} \rfloor}^{n_t+\lfloor \frac{W}{2} \rfloor} (y_{\text{smoothed}}[u] - \mu[n_t])^2, \quad \forall n_t \in \mathcal{N}, \quad (7)$$

where W is moving variance window size, $\lfloor \cdot \rfloor$ is the floor function which round down to the nearest integer, and $\mu[n_t]$ is the mean of the data points in the window for point n_t which can be defined as

$$\mu[n_t] = \frac{1}{W} \sum_{u=n_t-\lfloor \frac{W-1}{2} \rfloor}^{n_t+\lfloor \frac{W}{2} \rfloor} y_{\text{smoothed}}[u], \quad \forall n_t \in \mathcal{N}. \quad (8)$$

Now we use the calculated moving average to estimate $\hat{\mathcal{N}}$ using a threshold value γ as

$$\hat{\mathcal{N}} = \{n_t \mid v[n_t] \leq \gamma, \forall n_t \in \mathcal{N}\}. \quad (9)$$

IV. NUMERICAL RESULTS

In this section, we present selected numerical results. As stated in Section. II, we evaluate the performance of the methodology conducted for five distinct scenarios,

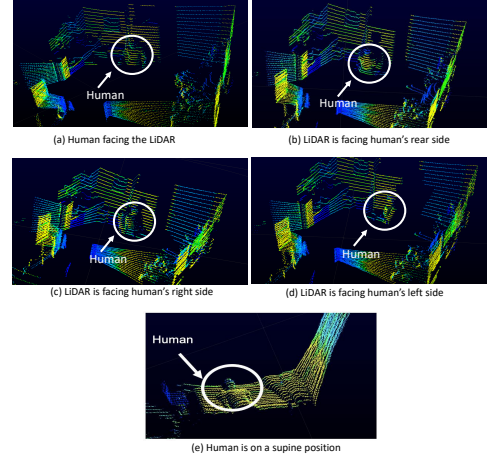


Fig. 5: Illustration of the conducted experimentation.

a snapshot of the raw collected data of these five scenarios is shown in Fig. 5, while we utilized the Velodyne PUCK LiDAR sensor to conduct all these measurements. We experimentally specified stationary ROI thresholds x_{th1} , x_{th2} , y_{th1} , y_{th2} , z_{th1} , and z_{th2} in a scenario-specific manner. The number of points per raw point cloud collected I , the number of the filtered point cloud E , and the number of time frames T are all dependent values based on the LiDAR measurement in every distinct scenario. The window size of the moving average window M in (4) is set to 10, while the window size of the moving variance window W in (7) is set to be 25. The threshold value for identifying the holding breath frames γ in (9) is set to 1×10^{-6} . Finally, this study was institutional review board (IRB) approved via University of Missouri human subjects research office.

As we collect four metrics in our methodology and that are (i) the frames of breathing set denoted by the set $\bar{\mathcal{N}}$, (ii) the frames of holding breath set denoted by the set $\hat{\mathcal{N}}$, (iii) the breathing depth denoted by the set $\bar{\mathcal{B}}$, and (iv) the respiratory rate denoted by R ; we use *Accuracy* to evaluate the first two metrics, while we use the *Root Mean Square Error (RMSE)* to evaluate the latter two. We define *Accuracy* as

$$\text{Accuracy} = \frac{TP + TN}{TP + TN + FP + FN}, \quad (10)$$

where TP refers to the true positive, TN refers to the true negative, FP refers to the false positive, and FN refers to the false negative. The *RMSE* is defined as

$$\text{RMSE} = \sqrt{\frac{1}{K} \sum_{k=1}^K (y_k - \hat{y}_k)^2}, \quad (11)$$

where y_k is the estimated value, and \hat{y}_k is the ground truth. For both metrics, we rely on manual ground truth constitution in which we manually specify the frames of breath, the frames of holding breath, the breath depth, and the respiratory rate based on our inspection of the data.

The experimental results are delineated in Table. I, which highlights the dependence of breathing performance metrics on the spatial alignment of the human subject with respect to the LiDAR sensor. Optimal breathing detection accuracy is reported for scenarios where the LiDAR is aligned with

TABLE I: Breathing monitoring numerical results

Scenario	Breathing Accuracy	Holding Breath Accuracy	Breath Depth RMSE	Respiratory rate RMSE
Scenario-a	1.00	0.93	0.0019	0.00
Scenario-b	0.73	0.85	0.0020	3.21
Scenario-c	0.87	0.89	0.0014	1.63
Scenario-d	0.93	0.92	0.0015	0.78
Scenario-e	1.00	0.94	0.0014	0.00

the front of the human subject (Scenario-a and Scenario-e). The rear-facing orientation (Scenario-b) resulted in the least accurate breathing performance, whereas side-facing orientations (Scenario-c and Scenario-d) delivered intermediate accuracy. This variation in performance can be attributed to the underlying detection mechanism, which is predicated on capturing the thoracic movements induced by respiration, movements that are more prominently manifested and hence more readily detected at the front of the torso than at the rear.

The RMSE associated with respiratory rate reflects the critical dependence on the detection precision of individual breath cycles. Misidentification or omission of a cycle can significantly skew the respiratory rate estimation, as articulated in (6). For the depth of breathing, the RMSE was calculated exclusively for correctly identified breathing cycles. This selective evaluation has yielded a lower RMSE for breathing depth, indicating a high fidelity in quantifying the amplitude of thoracic movements during respiration for each correctly detected cycle. It is important to note that while depth estimation is robust in the various scenarios, the overall reliability of respiratory monitoring is dependent on the accuracy of breath cycle detection.

Fig. 6 showcases the process of identifying breath-holding events in Scenario-a, following the methods outlined in (7) and (9). The red curve illustrates the smoothed data, and the green curve depicts its moving variance, indicating chest movement variability over time. A drop in moving variance below the threshold γ (the yellow dashed line) signals minimal chest movement, pointing to breath-holding. Despite the threshold γ 's sensitivity, as detailed in Table. I, this method effectively detects respiratory events, enabling real-time monitoring and swift responses in urgent care. This precision highlights our system's reliability and its value in clinical environments where accurate respiratory tracking is crucial.

V. CONCLUSION

This study explores LiDAR technology's effectiveness in remote breathing monitoring by converting torso movements into a signal that highlights various breathing metrics. Through experiments in five unique scenarios involving different subject orientations to the LiDAR sensor, we found that while subject orientation affects measurement accuracy, LiDAR reliably monitors respiration across all situations. This demonstrates LiDAR's robustness and adaptability for real-world use, where controlling subject-sensor positioning is challenging, confirming its potential for versatile respiratory monitoring applications.

REFERENCES

[1] M. Bahrami and M. Forouzanfar, "Sleep apnea detection from single-lead ECG: A comprehensive analysis of machine learning and deep

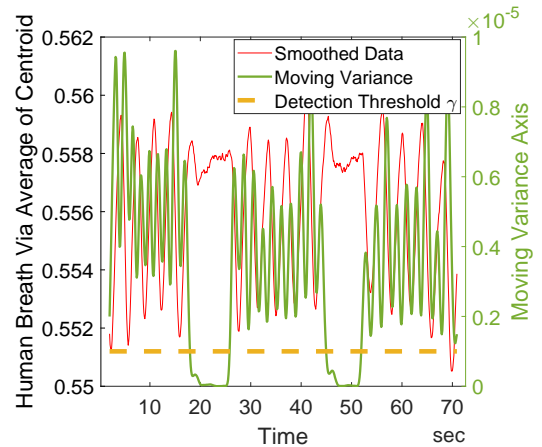


Fig. 6: Illustration of holding breath detection mechanism.

learning algorithms," *IEEE Transactions on Instrumentation and Measurement*, vol. 71, pp. 1–11, Feb. 2022.

[2] I. Costanzo, D. Sen, L. Rhein, and U. Guler, "Respiratory monitoring: Current state of the art and future roads," *IEEE Reviews in Biomedical Engineering*, vol. 15, pp. 103–121, Nov. 2022.

[3] C. Massaroni, J. Di Tocco, D. Lo Presti, U. G. Longo, S. Miccinilli, S. Sterzi, D. Formica, P. Saccomandi, and E. Schena, "Smart textile based on piezoresistive sensing elements for respiratory monitoring," *IEEE Sensors Journal*, vol. 19, no. 17, pp. 7718–7725, May 2019.

[4] D. A. Baker, "Four ironies of self-quantification: wearable technologies and the quantified self," *Science and engineering ethics*, vol. 26, no. 3, pp. 1477–1498, Jan. 2020.

[5] A. Procházka, H. Charvátová, O. Vyšata, J. Kopal, and J. Chambers, "Breathing analysis using thermal and depth imaging camera video records," *Sensors*, vol. 17, no. 6, pp. 1–10, June 2017.

[6] C. Massaroni, A. Nicolò, M. Sacchetti, and E. Schena, "Contactless methods for measuring respiratory rate: A review," *IEEE Sensors Journal*, vol. 21, no. 11, pp. 12821–12839, June 2021.

[7] C. James, A. Richardson, P. Watt, and N. Maxwell, "Reliability and validity of skin temperature measurement by telemetry thermistors and a thermal camera during exercise in the heat," *Journal of thermal biology*, vol. 45, pp. 141–149, Oct. 2014.

[8] B. Sinclair, "Kinect has problems recognizing dark-skinned users?" *GameSpot*, Nov. 2010. [Online]. Available: <https://www.gamespot.com/articles/kinect-has-problems-recognizing-dark-skinned-users/1100-6283514/>

[9] J. Angwin, J. Larson, S. Mattu, and L. Kirchner, *Machine Bias*. CRC Press, May 2022, ch. 6.1, pp. 1–11.

[10] M. Guariglia and C. Quintin, "Thermal imaging cameras are still dangerous dragnet surveillance cameras," *Electronic Frontier Foundation*, Apr. 2020. [Online]. Available: www.eff.org/deeplinks/2020/04/thermal-imaging-cameras-are-still-dangerous-drag-net-surveillance-cameras

[11] O. Rinchi, H. Ghazzai, A. Alsharoa, and Y. Massoud, "LiDAR technology for human activity recognition: Outlooks and challenges," *IEEE Internet of Things Magazine*, vol. 6, no. 2, pp. 143–150, June 2023.

[12] O. Rinchi, N. Nisbett, and A. Alsharoa, "Patients arms segmentation and gesture identification using standalone 3-D LiDAR sensors," *IEEE Sensors Letters*, vol. 7, no. 9, pp. 1–4, Aug. 2023.

[13] B. Hill, R. Stapley, M. S. Bin Nesar, and B. M. Whitaker, "Touchless respiratory monitor preliminary data and results," in *Proc. of the 25-th IEEE Aerospace Conference (AERO'21)*, Big Sky, MT, USA, Mar. 2021, pp. 1–7.

[14] M. S. Bin Nesar, K. Trippe, R. Stapley, B. M. Whitaker, and B. Hill, "Improving touchless respiratory monitoring via LiDAR orientation and thermal imaging," in *Proc. of the 26-th IEEE Aerospace Conference (AERO'22)*, Big Sky, MT, USA, Mar. 2022, pp. 1–8.

[15] B. Cherif, H. Ghazzai, A. Alsharoa, H. Besbes, and Y. Massoud, "Aerial LiDAR-based 3D object detection and tracking for traffic monitoring," in *Proc. of the 38-th IEEE International Symposium on Circuits and Systems (ISCAS'23)*, Monterey, CA, USA, May 2023, pp. 1–5.